Exploration of the interaction between dynein intermediate chain and dynactin p150^{Glued} reveals a novel binding interface

AJ Di Nicola, Bryn L. Romig, Stella M. Davis, Paul H. Cleary, Claire H. Yung, Daniel R. Marsan, Anna C. Merkt, Nikolaus M. Loening*

Department of Chemistry, Lewis & Clark College, 615 S Palatine Hill Road, Portland, OR 97219, United States

*Corresponding Author. Email: loening@lclark.edu

Abstract

Cytoplasmic dynein is a motor protein that plays a role in a number of cellular processes including retrograde transport. In many cases, dynein needs to interact with another protein, dynactin, to be fully active. An important step in the assembly of the dynein/dynactin complex is the interaction between the N-terminal portion of the intermediate chain (IC) subunit of dynein and the coiled-coil 1B (CC1B) region of the p150^{Glued} subunit of dynactin. Despite evidence for this interaction from binding studies, the exact location of where these proteins bind has remained elusive due to the dynamic nature of the interaction and the presence of intrinsically disordered regions in IC. By using intermolecular paramagnetic relaxation enhancements (PREs), we have been able to constrain the location of IC binding on p150^{Glued} to a position that is different from what has recently been hypothesized in a model of the dynein/dynactin complex based on cryo-electron microscopy (cryo-EM) data and AlphaFold predictions. In addition, although phosphorylation is important for regulating dynein/dynactin interactions, we show that a phosphomimetic mutation of IC is not sufficient to alter binding with p150^{Glued}.

Keywords

dynein intermediate chain, dynactin p150^{Glued}, nuclear magnetic resonance spectroscopy, isothermal titration calorimetry, phosphorylation, coiled-coils, intrinsically disordered proteins

Statements of impact for broader audience

One key interaction between the dynein motor protein and its co-factor dynactin occurs between the intermediate chain subunit of dynein and the p150^{Glued} subunit of dynactin. In this work, we localize the interface at which these proteins interact and show that this interaction is unaffected by a mutation that mimics phosphorylation.

Introduction

Found in most eukaryotic cells, the dynein family of motor proteins utilizes ATP hydrolysis to move along microtubules. Dyneins fall into two categories: axonemal dyneins, which contribute to generating movement in cilia and flagella, and cytoplasmic dyneins. Cytoplasmic dyneins play a role in integral cellular processes such as intracellular retrograde cargo transport, chromosome segregation during mitosis, and axonogenesis (1–3). In mammals, cytoplasmic dyneins consist of two heavy chains (HCs), two intermediate chains (ICs), two light intermediate chains, and several light chain dimers (LC7, LC8, and Tctex1) (3) as shown in Fig. 1. Both ATPase activity, which powers the movement of dynein along microtubules, and the site at which dynein binds microtubules are located in the HCs of the dynein complex (3–6).

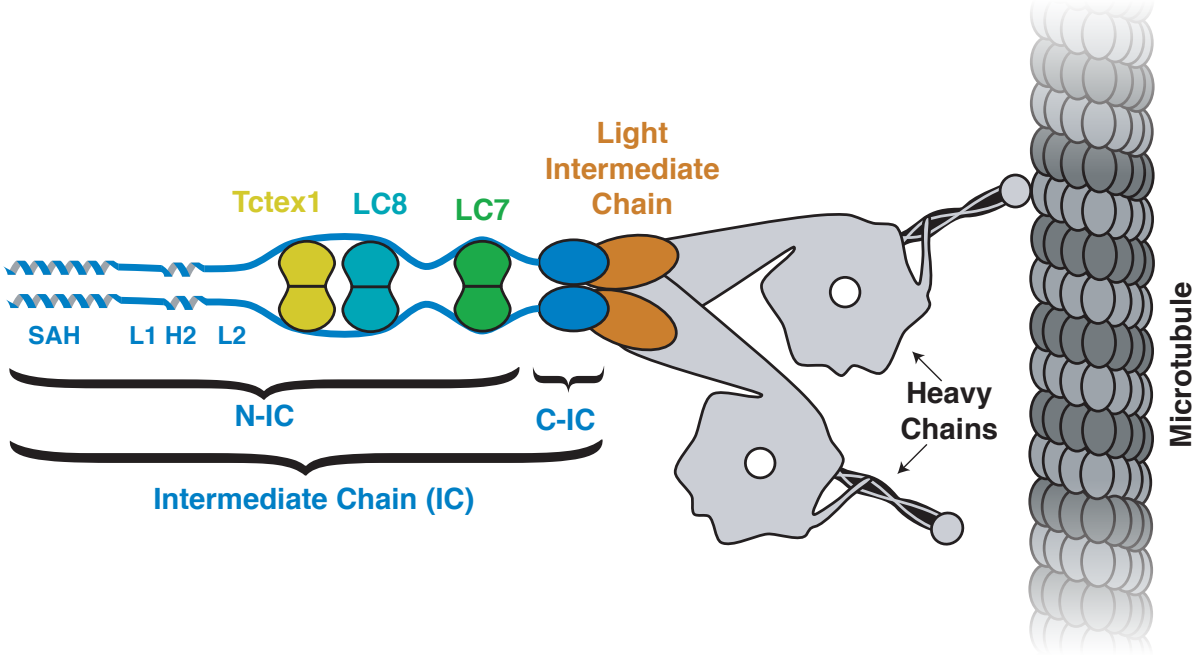

Figure 1. Cartoon representation of mammalian cytoplasmic dynein. Dynein consists of approximately 12 subunits: two heavy chains (gray), two light intermediate chains (orange), two intermediate chains (blue), and the light chain dimers LC7 (green), LC8 (teal), and Tctex1 (yellow).

The dynein ICs perform a multitude of functions, from governing interactions with dynein's regulatory partners to assisting in the assembly of the overall dynein complex (7–10). Mammalian cytoplasmic dynein HC and IC are each encoded by only two genes, indicating that the same components underlie all of cytoplasmic dynein's functions (11–13). Expression of the two IC genes in mice results in six isoforms of dynein IC-1, all of which are only or primarily located in neuronal tissue, and 11 isoforms of dynein IC-2 (13). Of the isoforms of IC expressed in mammals, we focus on IC-2C in this paper as it is the only isoform ubiquitously expressed throughout the body and the most well-studied of the IC isoforms (10, 14–16).

One key regulatory partner of cytoplasmic dynein is dynactin, which, like dynein, is a large multi-subunit protein complex. Mammalian cytoplasmic dynein only exhibits processive movement upon interacting with dynactin (17). Dynactin also facilitates dynein's binding with its cargo, highlighting the importance of dynactin for proper dynein functionality (17). Mutations that

disrupt the functionality of the dynein-dynactin complex in turn disrupt the ability of the cell to function properly. In *Drosophila melanogaster*, mutations in the HCs and ICs result in larval lethality (18, 19). Variants in IC-2 have been found to be related to microcephaly (20) and reduced levels of IC are linked to Alzheimer's disease (21). In dynactin, mutations in the p150Glued subunit have been linked to the neurodegenerative diseases lower motor neuron disease (MND) and Perry Syndrome (22). The implication of dysfunctional dynein and dynactin in neurodegenerative disease pathology emphasizes the importance of understanding the mechanisms that govern the interaction between these two proteins.

By directly interacting with each other, the IC subunit of dynein and the p150Glued subunit of dynactin regulate the overall dynein-dynactin interaction (see Fig. 2 for the domain architecture of these subunits) and one mechanism by which this interaction is regulated is phosphorylation (23, 24). Attempts to study the effect of phosphorylation by using phosphomimetic mutations have led to conflicting results as to its importance for IC/p150Glued binding (16, 23, 25). In the following, we will show that, at least in the context of the constructs used, the phosphomimetic mutation S84D in IC-2C does not alter interaction with p150Glued.

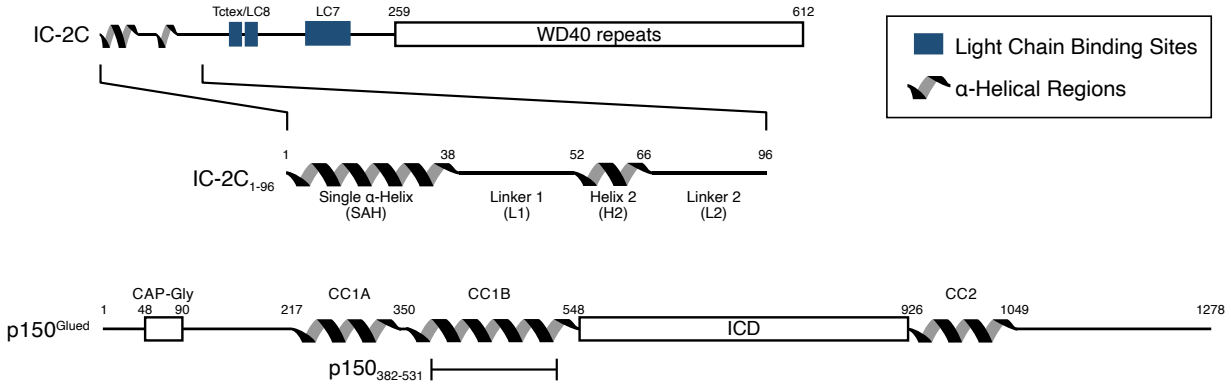

Figure 2. Domain architecture of mammalian IC-2C and p150Glued. The architecture for the IC-2C isoform of mammalian dynein IC is shown. IC-2C has binding sites for the dynein light chains (Tctex, LC8, LC7) and a series of WD40 repeats at the C-terminus that forms a β-propeller that interacts with the dynein HCs. The N-terminus of IC contains two α-helical regions (SAH and H2) and two disordered linker regions (L1 and L2). In p150Glued, CC1 and CC2 indicate two coiled-coil regions; CC1 is further divided into two subregions (CC1A and CC1B). Other folded domains of p150Glued are the intercoiled domain (ICD) and the cytoskeleton-associated protein/glycine-rich domain (CAP-Gly). IC-2C1-96 and p150382-531 are the constructs used for most of our work. Numbers indicate position in the amino acid sequence.

Previous research has established that it is the single α-helix (SAH) region in the N-terminus of IC (N-IC) that interacts with a subset of residues 382-531 in the coiled-coil 1B (CC1B) region of p150Glued (26, 27). The binding stoichiometry of the IC/p150Glued interaction suggests that two monomers of IC bind to one homodimer of p150Glued with the N-IC and CC1B regions forming a four-helix bundle, implying that the IC binding site on p150Glued CC1B should be no more than 30 amino acids long to match the size of the IC SAH region (27). The specific residues in CC1B involved in binding IC are unknown, and more detailed structural information about the N-IC/CC1B complex has been elusive. The characteristics of the N-IC/CC1B complex make it difficult to study, as dynamic and/or disordered regions are not amenable to crystallization for

x-ray crystallography and result in low electron density in cryo-electron microscopy (cryo-EM) maps. Initially, structural characterization via cryo-EM of a dynein-dynactin complex stabilized with bicaudal D2 (BICD2), another protein complex, failed to reveal information about the IC/p150^{Glued} interaction (28). As N-IC is intrinsically disordered in all but the α-helical SAH and helix 2 (H2) regions, the interaction between N-IC and p150^{Glued} is typically too dynamic to show electron density in cryo-EM maps (28, 29). This situation has improved with a recent model of the dynein/dynactin complex in combination with the regulator factor LIS1 (lissencephaly-1) protein based on cryo-EM data (30), which shows several details of the interaction between IC and p150^{Glued}. However, as we will show in this paper, our data suggest a different location for the binding interaction between N-IC and the CC1B region of p150^{Glued}.

Whereas x-ray crystallography and cryo-EM typically fail to provide details about intrinsically disordered regions of proteins, nuclear magnetic resonance (NMR) spectroscopy is able to provide atomic-level details about both structured and disordered regions of proteins (31–33). However, solution-state NMR studies of proteins are typically limited to smaller proteins, as the slower correlation times of larger proteins result in peak broadening that eventually makes NMR untenable. The constructs that are the focus of this work, p150$_{382\text{-}531}$ and IC-2C$_{1\text{-}96}$ (Fig. 2), are 150 and 96 residues long, respectively, and previous research suggests that the interaction between dimeric p150$_{382\text{-}531}$ and monomeric IC-2C$_{1\text{-}96}$ forms a four-helix bundle (27) resulting in a complex containing 492 residues (56.8 kDa). This is a rather large protein for NMR spectroscopy, and the spectra for this complex are made worse by the anisotropic tumbling of the coiled-coil p150$_{382\text{-}531}$ dimer, which leads to additional peak broadening, especially of the amide protons (34, 35).

To sidestep problems due to peak broadening, we have studied the interaction between p150$_{382\text{-}531}$ and IC-2C$_{1\text{-}96}$ via an indirect method that looks at how the bound state of these proteins (which is invisible in NMR spectra due to its size) influences the NMR spectra of free IC-2C$_{1\text{-}96}$. To do this, we attached paramagnetic labels at various locations along the p150$_{382\text{-}531}$ coiled-coil and then gathered NMR spectra from a series of samples containing p150$_{382\text{-}531}$ with a paramagnetic label at a specific site along with an excess of IC-2C$_{1\text{-}96}$. The exchange of IC-2C$_{1\text{-}96}$ between free and bound states means that the nuclear spin relaxation rates measured for the NMR peaks of the visible free state of IC-2C$_{1\text{-}96}$ are influenced by relaxation processes that affect the invisible bound state, and the paramagnetic label on p150$_{382\text{-}531}$ further increases the relaxation rates for IC-2C$_{1\text{-}96}$. This increase in relaxation rate due to the paramagnetic label is known as the paramagnetic relaxation enhancement (PRE) and has an r^{-6} dependence on the distance between the affected nuclei and the paramagnetic label (36). Typically, PREs are best determined using proton transverse relaxation rates (^{1}H R_2) and are defined as the difference in relaxation rates (Γ_2) between when the sample is in a paramagnetic state and after the paramagnetic label has been reduced to a diamagnetic state:

$$\Gamma_2 = R_{2,\text{paramagnetic}} - R_{2,\text{diamagnetic}} \quad (1)$$

As we will show in this paper, by moving the location of the paramagnetic label on p150$_{382\text{-}531}$, we were able to map out what range of residues of p150$_{382\text{-}531}$ interact with IC-2C$_{1\text{-}96}$ due to the variation in the intermolecular PREs between these proteins.

Results and discussion

The stability of the p150$_{382-531}$ construct is highly sensitive to temperature and ionic strength

The construct that we used to study the p150^{Glued} CC1B region (p150$_{382-531}$) has previously been identified to form a minimal fragment for binding dynein IC, with smaller constructs not exhibiting binding to IC-2C (27). To optimize the temperature and buffer conditions to be used for studying p150^{Glued}/IC binding, we used CD spectroscopy to measure the thermal denaturation temperature for p150$_{382-531}$ as a function of ionic strength (Fig. 3). At very low salt concentrations (0 mM NaCl, 10 mM phosphate), the CD signal is consistent with a structure that is a mixture of α-helical and disordered regions down to a temperature of 5ºC. Increasing the ionic strength by adding NaCl helps stabilize the structure, leading to CD spectra at low temperatures for which the ratio of the molar ellipticities at 222 and 208 nm is greater than unity, which is characteristic of coiled-coil structures (37). The denaturation midpoint temperature (T_m) for the coiled-coil structure increases with increasing ionic strength and changes most drastically going from 50 mM to 100 mM NaCl. The T_m value of 16.3 (±0.5)ºC at 150 mM NaCl/10 mM phosphate (pH 7.4) that we observed is roughly 3ºC higher than a previous CD-based thermal denaturing measurement for this construct taken using similar (but not identical) buffer conditions and a lower concentration of protein in the cuvette (27).

We found that the folding of p150$_{382-531}$ is easily reversible; most of the data in Fig. 3 were acquired using the same sample to which a small volume of 5 M NaCl was added to increase the ionic strength between each set of variable-temperature CD spectra. In addition, we have at times purified p150$_{382-531}$ using SEC with a denaturing running buffer containing 1 M guanidinium chloride and have been able to recover the coiled-coil structure after buffer exchange into a non-denaturing buffer (data not shown). This reversibility of folding is not surprising considering the simplicity of the coiled-coil structure and is in agreement with a previous group (29) that studied a slightly larger construct (p150$_{358-555}$).

Although we found that p150$_{382-531}$ stability is slightly improved by going to salt concentrations above 150 mM NaCl, we decided to use 150 mM NaCl/50 mM phosphate (pH 7.4) for subsequent experiments, as this buffer condition roughly matches physiological ionic strength and pH and matches the buffer used for the final step of purification (SEC). The marginal stability of the p150$_{382-531}$ coiled-coil structure explains why binding with IC was not observed for smaller constructs of p150^{Glued} in previous studies (27), as smaller constructs will be destabilized to the point that their coiled-coil structures will fail to form at all temperatures and salt concentrations.

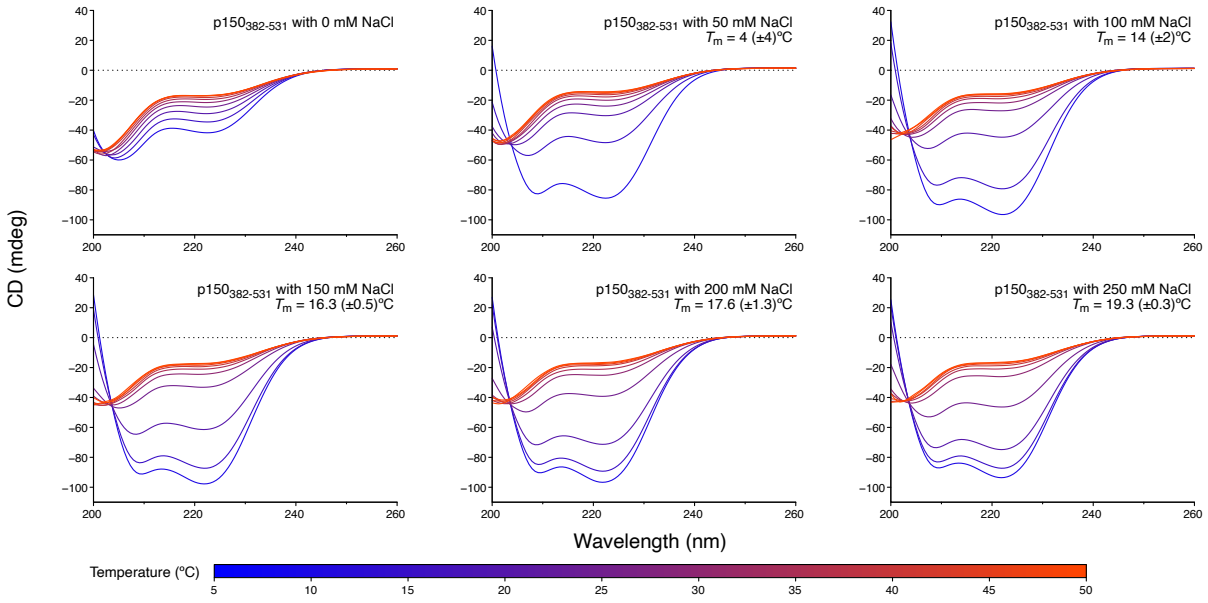

Figure 3. The thermal stability of the coiled-coiled structure of p150$_{382-531}$ varies with ionic strength. All samples were at ≈15 µM in 10 mM sodium phosphate (pH 7.4) with 0 to 250 mM NaCl. CD spectra were collected at 5º intervals from 5 to 50°C. The denaturation midpoint temperature (T_m) for 150 mM NaCl [16.3 (±0.5)ºC] differs from that in Fig. S1 [20.2 (±0.4)ºC] due to differences in sample concentration and buffer composition (10 mM here versus 50 mM phosphate for Fig. S1).

We used ITC to measure the dissociation constant (K_d) for the p150$_{382-531}$ dimer at temperatures ranging from 5ºC up to 30ºC (Fig. 4a). To do this, p150$_{382-531}$ at a high concentration in the ITC syringe was injected into a cell containing only buffer, resulting in endothermic peaks due to p150$_{382-531}$ dimers dissociating after each injection. The results at both high and low temperatures (5, 10, and 30ºC) are noisy due to the relatively small amounts of heat absorbed per injection compared to the runs at intermediate temperatures, leading to large errors for the estimated K_d values at the high and low temperatures. At 30ºC, this unreliability is because p150$_{382-531}$ is already mostly a monomer even at the high concentration in the syringe, so relatively little additional dissociation occurs upon injection/dilution into the cell. At low temperatures (5 and 10ºC), the p150$_{382-531}$ dimer is stable enough that little dissociation occurs after injection into the cell, so relatively little heat is absorbed. In addition, the results at low temperatures are confounded by higher-order oligomerization of p150$_{382-531}$ at the high concentrations in the syringe, leading to endothermic effects upon dilution that obscure the actual dimer/monomer equilibrium.

A previous group used sedimentation equilibrium analytical ultracentrifugation (SE-AUC) to determine that the K_d for p150$_{382-531}$ is less than 0.060 µM at 4ºC (27), a result which is in line with our data at higher temperatures if the unreliable ITC results at 5 and 10ºC are ignored (Fig. 4b). All subsequent ITC experiments exploring IC/p150^{Glued} binding were carried out at 15ºC under conditions in which the p150$_{382-531}$ was at concentrations in the cell above the K_d for p150$_{382-531}$ dimerization at this temperature.

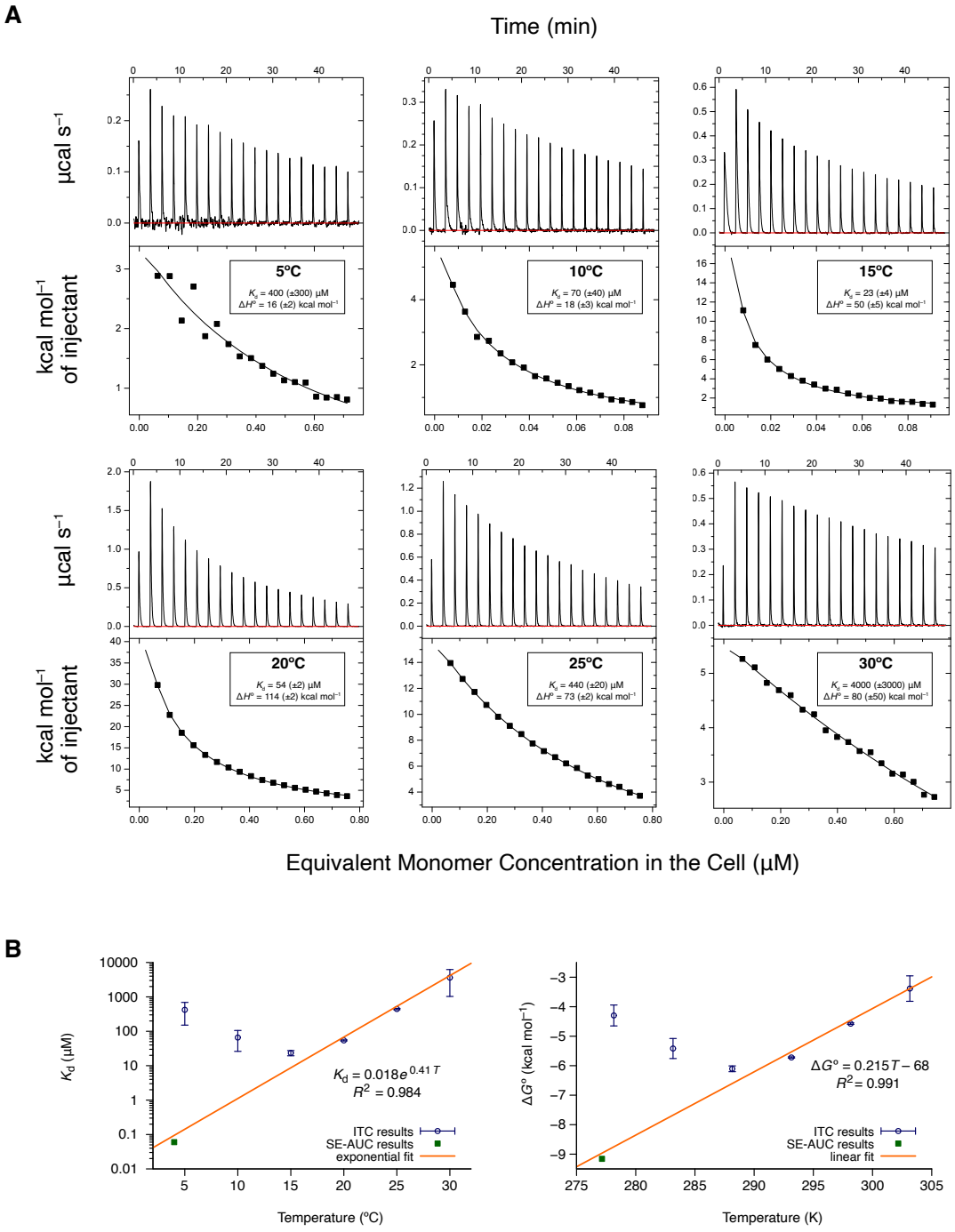

Figure 4. The stability of the p150$_{382-531}$ dimer is highly temperature-dependent. (a) Representative thermograms (top) and binding isotherms (bottom) from ITC titrations of p150$_{382-531}$ WT into buffer. Thermodynamic parameters at 10 and 15°C are the average of three replicates with their standard deviations, whereas the values for other temperatures are from single measurements with errors from the curve fit. (b) Comparison of K_d and $\Delta G°$ values for p150$_{382-531}$ WT acquired using ITC (blue circles) and SE-AUC [green squares, from ref. (27)]. The ITC data at 15, 20, 25, and 30°C, along with the SE-AUC data at 4°C, were fit using linear least squares. The ITC data at 5 and 10°C (and to a small extent, 15°C) deviate from the expected trend because of other processes obscuring the small amount of heat absorbed by the dimer/monomer equilibrium at these temperatures.

The p150^{Glued} binding site on IC-2C$_{1-96}$ only involves the SAH region

Although recent work with IC and p150^{Glued} from *Chaetomium thermophilum* has shown that both the SAH and H2 regions of IC are involved in binding with p150^{Glued} (38), it is believed that for the *Drosophila melanogaster* and mammalian versions of IC and p150^{Glued} only the SAH region of IC is involved in binding p150^{Glued}, as constructs containing only the SAH region bind with similar affinity for p150^{Glued} as constructs that contain both regions (26, 27). Interestingly, when unlabeled p150$_{382-531}$ is titrated into ^{15}N-labeled IC-2C$_{1-96}$ (Fig. 5a), we observed reduced NMR signals for residues in both the SAH and H2 regions. However, the reduction in peak heights for amides in the H2 region could be caused by an indirect effect due to an interaction between the SAH/H2 regions rather than being caused by a direct interaction with p150$_{382-531}$.

To confirm that only the SAH region is involved in the IC/p150^{Glued} interaction for mammalian proteins, we generated a construct of IC-2C that contained the L1, H2, and L2 regions but did not contain the SAH region (IC-2C$_{38-96}$). NMR spectra of ^{15}N-labeled IC-2C$_{38-96}$ with and without unlabeled p150$_{382-531}$ showed no differences (Fig. 5b), which directly establishes that only the SAH region of IC-2C$_{1-96}$ is involved in binding p150$_{382-531}$ and strongly suggests that the size of the binding site for IC-2C on p150$_{382-531}$ should only be as large (or possibly smaller) than the IC-2C SAH region.

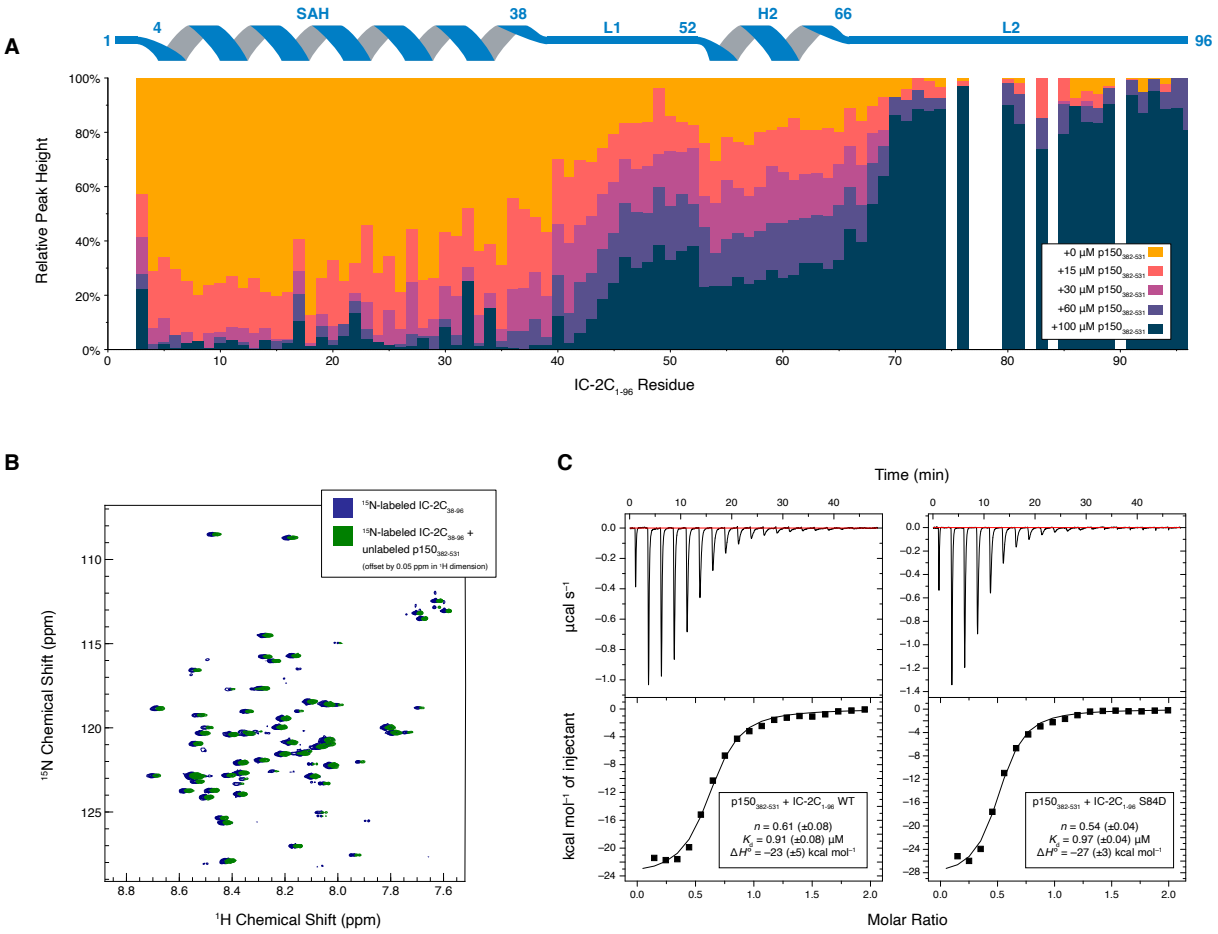

Figure 5. The H2 region of IC-2C$_{1-96}$ does not bind to p150$_{382-531}$ and the S84D phosphomimetic mutation does not alter binding of IC-2C$_{1-96}$ with p150$_{382-531}$. (a) NMR titration of ^{15}N-labeled IC-2C$_{1-96}$ at 300 μM with unlabeled p150$_{382-531}$. The peak height for each amide is shown relative to its height when no p150$_{382-531}$ is added. Large reductions in peak height are observed for amides in the SAH region upon addition of p150$_{382-531}$; smaller reductions are also observed for amides in the H2 region. (b) ^{1}H-^{15}N HSQC spectra of 165 μM ^{15}N-labeled IC-2C$_{38-96}$ without (blue) and with (green) an equimolar amount of unlabeled p150$_{382-531}$. The lack of changes in peak intensities and peak positions between the two spectra indicates the absence of a binding interaction between IC-2C$_{38-96}$ and p150$_{382-531}$. The spectrum of IC-2C$_{38-96}$ with p150$_{382-531}$ added is deliberately offset by 0.05 ppm in the ^{1}H dimension to help visualize overlapping peaks. (c) Representative thermograms (top) and binding isotherms (bottom) of IC-2C$_{1-96}$ WT (left) and S84D (right) titrated into p150$_{382-531}$ WT result in thermodynamic parameters that are not significantly different. Thermodynamic parameters are the average of three replicates with their standard deviations.

The phosphomimetic S84D mutation does not affect p150^{Glued}/IC binding

Although phosphorylation of rat IC-2C at S84 was previously shown to block p150^{Glued} binding in blot overlay assays (23), attempts to further clarify this interaction using S84A mutants (which cannot be phosphorylated) and S84D mutants (which mimic phosphorylation, although with only a –1 charge rather than a –2 charge) both in vivo and in vitro have led to conflicting results as to

the importance of S84 phosphorylation for regulating p150^{Glued} binding (23, 25). A more recent study claimed to show that the S84D mutation in IC-2C$_{1-96}$ disrupts binding with p150^{Glued} but does not affect binding with Nudel (16). However, we have come to believe that the results from that more recent study in regard to the effect of S84D on IC/p150^{Glued} binding are incorrect. First, in stark contrast to the ITC results that were previously reported, we observed no significant difference between WT and S84D versions of IC-2C$_{1-96}$ for the binding interaction with p150$_{382-531}$ both using conditions at which the p150$_{382-531}$ coiled-coil is mostly fully-formed (Fig. 5c) and using the previous conditions (25ºC, 50 mM NaCl) for which the interaction is 10-fold weaker because the p150$_{382-531}$ coiled-coil is mostly denatured (data not shown). Second, the previous study always had a binding stoichiometry of ~1.0, whereas we have always found the binding stoichiometry to be closer to 0.5. The reasons for the lower binding stoichiometry will be discussed later in this paper, but we believe that the value used for the concentration of IC-2C (which is difficult to quantify due to a lack of absorbance at 280 nm) was adjusted during fitting to get the "expected" ~1.0 binding stoichiometry. Third, the previous study presented NMR data that suggested that the S84D mutation caused chemical shift perturbations for amides in the SAH and H2 regions of IC-2C and therefore concluded that the S84D mutation changed the overall conformation of IC-2C. However, we did not observe these chemical shift perturbations when comparing NMR spectra for IC-2C$_{1-96}$ WT and IC-2C$_{1-96}$ S84D. Instead, the perturbations exactly matched changes that we observed when varying the NaCl concentration for IC-2C$_{1-96}$ WT. Consequently, we believe the previous study mistakenly attributed spectrum changes to the S84D mutation that were actually due to variations in the ionic strength of the samples.

Our results show that, at least in the context of the IC-2C$_{1-96}$ and p150$_{382-531}$ constructs that we studied, the S84D mutation in IC-2C$_{1-96}$ does not affect IC/p150^{Glued} binding (Fig. 5c). There are a few possible conclusions that can be drawn from this result. First, it is possible that phosphorylation at S84 does not have an effect on IC/p150^{Glued} binding. However, that seems unlikely based on the strength of previous evidence demonstrating the importance of S84 phosphorylation (23). Second, it could be that the smaller charge of the S84D phosphomimetic mutation is not large enough to produce the same effect as true phosphorylation in this system. However, that also seems unlikely, as we should still expect some changes in the ITC and NMR data (albeit smaller variations than would be expected with true phosphorylation) rather than a complete absence of an effect. The third possible conclusion, which we believe most likely and has been previously suggested (25) to explain the seemingly contradictory results for S84D phosphomimetic mutations (23, 25), is that the importance of phosphorylation of S84 (and the effect of S84D phosphomimetic mutations) might be due to a secondary binding site that is only present in IC-2C and p150^{Glued} constructs larger than the ones we studied.

Single-cysteine mutations and MTSL-labeling does not significantly impact the coiled-coil structure of p150$_{352-531}$ or its binding with IC-2C$_{1-96}$

We used a number of algorithms for coiled-coil structure prediction to identify locations in p150$_{382-531}$ (which does not have any native cysteine residues) that could be mutated to cysteine without altering the overall structure so that the resulting mutants could be labeled with the paramagnetic MTSL tag. Whereas α-helices on their own usually have 3.6 residues per turn of the helix, α-helices in coiled-coils are wound a little less tightly, with only 3.5 residues per turn. This means that seven amino acids (a heptad, with positions labeled *abcdefg*) correspond to two complete turns of a coiled-coil helix. The *a* and *d* positions of the heptad form the interface between the two α-helices of a coiled-coil dimer; the amino acids found at these positions are typically

hydrophobic (most commonly L, I, V, M, Y, or A) (39). The amino acids in the other five positions tend to be polar, and salt bridges between charged residues in positions *e* and *g* can provide additional stabilization of the coiled-coil structure.

In our mutagenesis design, we used the WaggaWagga website (40) to identify several hydrophobic or nonpolar residues that are predicted to face away from the coiled-coil dimer interface. By doing so, we were able to introduce cysteine mutations at residues that are not predicted to form the coiled-coil dimer interface (positions *a* and *d*) and also avoid mutating charged residues that could potentially disrupt salt bridges that provide the dimer with additional stability. Fig. 6 shows the locations identified for introducing cysteine mutations, along with the predicted heptad pattern for $p150_{382\text{-}531}$ from the Marcoil (41), MultiCoil2 (42), NCOILS (43), PairCoil2 (44), PCOILS (45), and DeepCoil2 (46) programs as well as the heptad repeat pattern determined from three-dimensional structures predicted by AlphaFold3 (47). As there were disagreements in the heptad structure between the various algorithms, we selected sites for mutagenesis that avoided the *a* and *d* positions in all of the predictions.

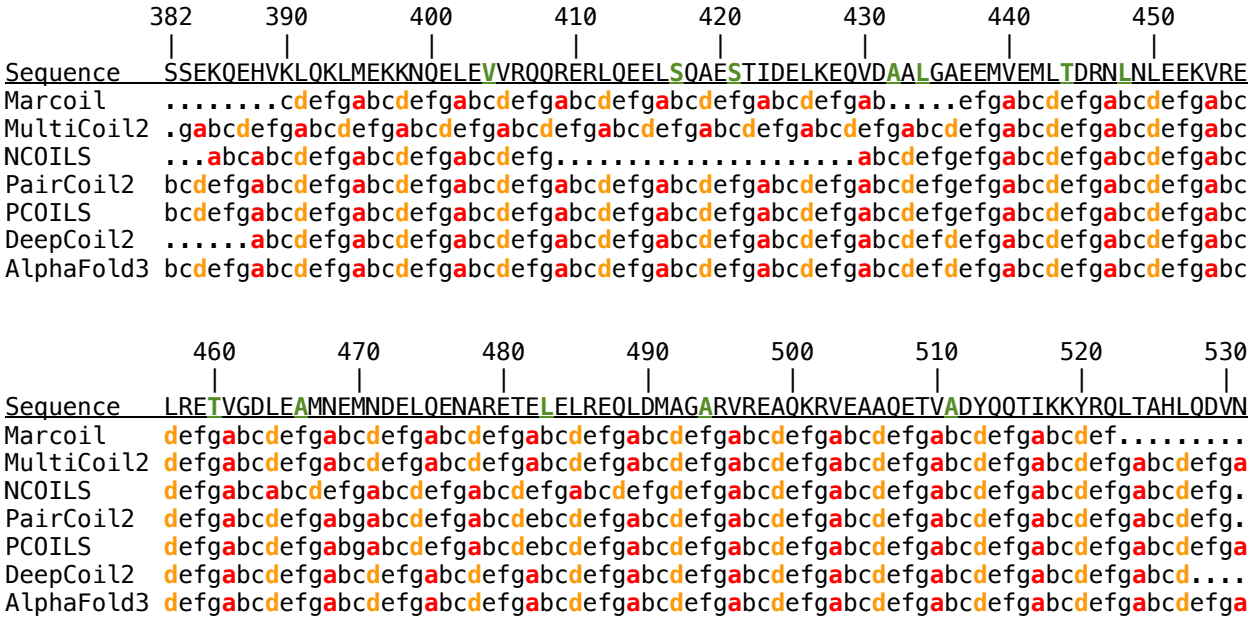

Figure 6. A variety of coiled-coil structure prediction methods were used to identify locations for generating single-cysteine mutants of $p150_{382\text{-}531}$. For mutagenesis, residues in positions *a* (red letters) and *d* (gold letters) in the coiled-coil heptad repeat were avoided as these form the coiled-coil dimer interface; the 12 sites for which we eventually generated single cysteine mutations are indicated in green. DeepCoil2 only predicts *a* and *d* sites; other heptad positions were inferred based on those. The heptad positions from the AlphaFold3 prediction are based on visual inspection of the three-dimensional structures that it generated.

We used temperature-dependent CD spectroscopy to assess whether the introduction of each cysteine mutation and subsequent MTSL labeling significantly impacted the secondary structure of the $p150_{382\text{-}531}$ constructs. As shown in Fig. S1, $p150_{382\text{-}531}$ wild-type (WT) and MTSL-labeled single-cysteine mutants of $p150_{382\text{-}531}$ have very similar CD spectra, suggesting that the mutations and MTSL-labeling had little, if any, effect on the secondary structure or the thermal stability of the constructs. Careful analysis of the average mean ellipticity from 220 to 224 nm for

each sample at each temperature (Fig. S1, top right) does show some small variations in the estimated denaturation midpoint temperatures (T_m). These variations could possibly be due to small changes in structure/stability of the constructs but are more likely due to small variations in the sample concentration and buffer conditions from sample to sample.

The interaction between p150$_{382-531}$ and IC-2C$_{1-96}$ is believed to be driven by electrostatic interactions (27), so our mutagenesis strategy for generating single-cysteine p150$_{382-531}$ mutants avoided changing charged residues. Even so, more subtle intermolecular interactions along with steric effects due to the addition of the MTSL label could alter binding, so we used ITC to assess whether the MTSL-labeled single-cysteine mutants of p150$_{382-531}$ had binding affinities with IC-2C$_{1-96}$ that were similar to p150$_{382-531}$ WT. Our ITC runs at 15ºC (Fig. S2) typically resulted in values of $n \sim 0.5$, $K_d \sim 1$ μM, and $\Delta H \sim -25$ kcal mol^{-1}. The errors provided in Fig. S2 are the fit errors for individual thermograms and therefore underestimate the true errors for the thermodynamic values. This is because the accuracy of our ITC results is fundamentally limited by the accuracy of our A$_{205}$ and A$_{280}$-based concentration measurements, which without careful calibration are limited by the assumptions built into using calculated ε_{205} and ε_{280} values to determine protein concentrations (48), and because of batch-to-batch variations in protein purity. In most cases, the variations between samples are small enough that they are more likely due to variations in sample preparation/purity rather than to meaningful changes in the binding interaction. Even for MTSL-labeled single-cysteine mutants for which the binding interaction did seem to weaken (such as p150$_{382-531}$ T460C), the changes were not large enough to undermine the intermolecular PRE results discussed later in this paper as the large number of single-cysteine mutants used provides redundancy to our conclusions.

Most of the ITC thermograms (Fig. 5c, S2) show an initial dip indicating that a more complicated interaction is occurring than can be properly fit with the one-site model that we used for interpreting the data. Although using a more complicated model (like a two-site model) did provide visually better fits, it greatly increased the uncertainty in the fitting parameters, and the results were sensitive to the initial parameter estimates. As our goal here was to ensure that the IC/p150^{Glued} binding behavior was broadly the same regardless of which single-cysteine mutant was used, rather than to develop a sophisticated model of the binding interaction and to precisely characterize the thermodynamics of each step in binding, we proceeded to use a one-site model to facilitate making broad comparisons between samples.

Substoichiometric binding is observed in the IC-2C$_{1-96}$/p150$_{352-531}$ interaction

Based on their results from SE-AUC, previous researchers suggested that the N-IC/p150$_{382-531}$ complex was heterotetrameric and bound in a 2:2 ratio with two monomers of IC-2C$_{1-124}$ binding to one homodimer of p150$_{382-531}$ (27). This binding stoichiometry makes intuitive sense as, based on symmetry considerations, the coiled-coil structure of the p150$_{382-531}$ homodimer should have two equivalent binding sites for IC. If IC and p150$_{382-531}$ bind in a 2:2 ratio, the theoretical binding stoichiometry (n) of our ITC binding affinity experiments with IC-2C$_{1-96}$ and p150$_{382-531}$ should be 1.0. However, we invariably observed an experimental binding stoichiometry between 0.5 and 0.7 (Fig. 5c, S2), implying that approximately one N-IC monomer binds to one p150$_{382-531}$ dimer.

As controls, we carried out ITC experiments using a second instrument and also using different concentrations of IC-2C$_{1-96}$ and p150$_{382-531}$ (Fig. S3). We found that the binding stoichiometry and dissociation constant remained the same between instruments and across sample concentrations. As noted in our previous ITC results (Fig. 5c, S2), we continued to observe that the ITC results were not adequately fit by a one-site model (as seen by the behavior of the first few

data points in the binding isotherms, particularly at high concentrations). We believe that the most likely explanation is that there is an endothermic penalty for rearranging the p150$_{382-531}$ dimer when IC-2C$_{1-96}$ binds to it. The penalty becomes smaller at lower concentrations because the dimer-monomer equilibrium for p150$_{382-531}$ is shifted more toward the monomer side of the equilibrium. This also explains why the binding interaction appears to become more exothermic when lower concentrations of protein are used (Fig. S3).

As for the substoichiometric binding constant ($n < 1$), we hypothesize that this is because inserting the first copy of IC-2C$_{1-96}$ into the p150$_{382-531}$ coiled-coil dimer causes a rearrangement of the dimer that breaks its symmetry, thereby weakening the second IC-2C$_{1-96}$ binding site on the p150$_{382-531}$ coiled-coil. In agreement with our results, substoichiometric binding between the monomeric SAH region of IC (IC-2C$_{1-32}$) and dimeric p150^{Glued} CC1B was also recently observed in GST (glutathione S-transferase) pull-down assays (30). In that work, stoichiometric binding was only achieved when the assay was changed to greatly increase the local concentration of IC, which was hypothesized to more closely match the behavior of the fully formed dynein motor protein complex (a system in which IC is a dimer and therefore two copies of the SAH region are forced to be in close proximity).

Intermolecular PRE results suggest that the IC-2C binding site on p150^{Glued} CC1B includes residues 432–448

We used measurements of intermolecular PREs to determine the location of the IC-2C binding site on p150$_{382-531}$. To do this, we carried out NMR experiments that measured the transverse relaxation rates for amide protons (^{1}H R_2) of ^{15}N-labeled IC-2C$_{1-96}$ in the presence of MTSL-labeled p150$_{382-531}$ single-cysteine mutants. As binding with p150$_{382-531}$ causes the NMR signals for residues in the SAH and H2 regions of IC-2C$_{1-96}$ to disappear (Fig. 5a), we first needed to optimize the ratio of these proteins so that we would have a measurable PRE effect from the MTSL-labeled p150$_{382-531}$ while still having enough signal from amides in the SAH and H2 regions of IC-2C$_{1-96}$ to be able to accurately quantify the relaxation rates. As seen in Fig. S4, a p150$_{382-531}$/IC-2C$_{1-96}$ ratio of 1:40 still had a measurable PRE effect while also allowing us to observe peaks for all residues in the SAH region and resulted in more accurate relaxation rates than samples with higher concentrations of p150$_{382-531}$ (1:20 and 1:10 ratios).

Using a 1:40 p150$_{382-531}$/IC-2C$_{1-96}$ ratio, we carried out intermolecular PRE measurements for 12 different MTSL-labeled single-cysteine mutants of p150$_{382-531}$ (Fig. S5). To help summarize this PRE data, we used it to calculate the average PRE for each IC-2C$_{1-96}$ region using residues 5-35 for the SAH region, 40-50 for the L1 region, 55-65 for the H2 region, and 70-95 for the L2 region. These averaged results (Fig. 7) show that the PREs for residues in the SAH region of IC-2C$_{1-96}$ were largest when the MTSL label was at residues 432, 434, 444, and 448 in p150$_{382-531}$ and had a much smaller impact for all other regions of IC-2C$_{1-96}$. A small increase in average PRE value for residues in the SAH region is generally seen for the other mutants, reflecting longer-range interactions or transient/weaker interactions with those parts of p150$_{382-531}$. Interestingly, attaching the MTSL label at residue 511 in p150$_{382-531}$ showed an increase in the average PRE for the H2 region of IC-2C$_{1-96}$ even though we have established that this region does not directly bind to p150$_{382-531}$ (Fig. 5b).

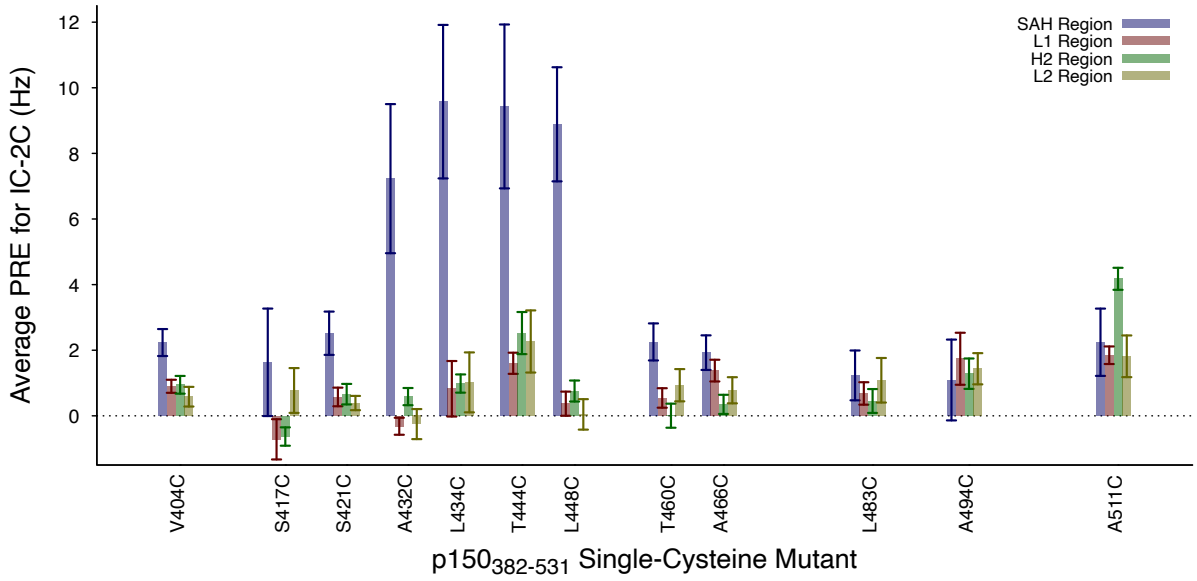

Figure 7. The largest average PREs for residues in the single α-helix (SAH) region of IC-2C$_{1\text{-}96}$ occur when the MTSL label is attached at residues 432, 434, 444, and 448 in p150$_{382\text{-}531}$. The average PRE (Γ_2) for each IC-2C$_{1\text{-}96}$ region was calculated by averaging the PRE values for selected residues in each region: residues 5-35 for SAH (blue); 40-50 for L1 (red); 55-65 for H2 (green); and 70-95 for L2 (yellow). The spacing on the *x*-axis reflects the distances between the different cysteine mutation sites along the p150$_{382\text{-}531}$ coiled-coil structure. Error bars denote the standard deviation of the mean. See Fig. S5 for ^{1}H R_2 graphs for each individual single-cysteine mutant.

These results show that the main IC-2C binding site on p150^{Glued} includes residues 432 to 448 of p150^{Glued} but does not include residues 421 and below or 460 and above. Similarly, the site of p150^{Glued} binding on IC-2C is constrained to be between residues 5-35. Whether the binding interaction between the two proteins entails a full ~30 residues (425-455 for p150^{Glued}, 5-35 for IC-2C) or a smaller number of residues within these ranges is not clear from our data and will depend on the angle formed between the IC-2C SAH and the p150^{Glued} coiled-coil. However, the data do suggest that the helices are positioned in a parallel (rather than anti-parallel) orientation. This is shown by the slightly larger PREs for the N-terminal residues of the SAH region when the MTSL label is at residue 432 or 434 of p150^{Glued} and for the C-terminal residues of the SAH region when the MTSL label is at residue 444 or 448 (Fig. S5). In addition, the PRE observed for the H2 region of IC-2C when the MTSL label is at residue 511 is consistent with a parallel orientation as the H2 region will be sterically constrained to be near that part of p150^{Glued} (even if H2 does not actually bind to p150^{Glued}) because it is tethered to the IC-2C SAH region by the L1 linker. Interestingly, algorithms for predicting coiled-coils (Fig. 6) predict some deviations in the coiled-coil heptad motif within the region of p150^{Glued} where IC binds. We hypothesize that this provides flexibility in the coiled-coil structure so that p150^{Glued} can rearrange to accommodate binding to IC. Taken together, the PRE results are consistent with the schematic model shown in Fig. 8.

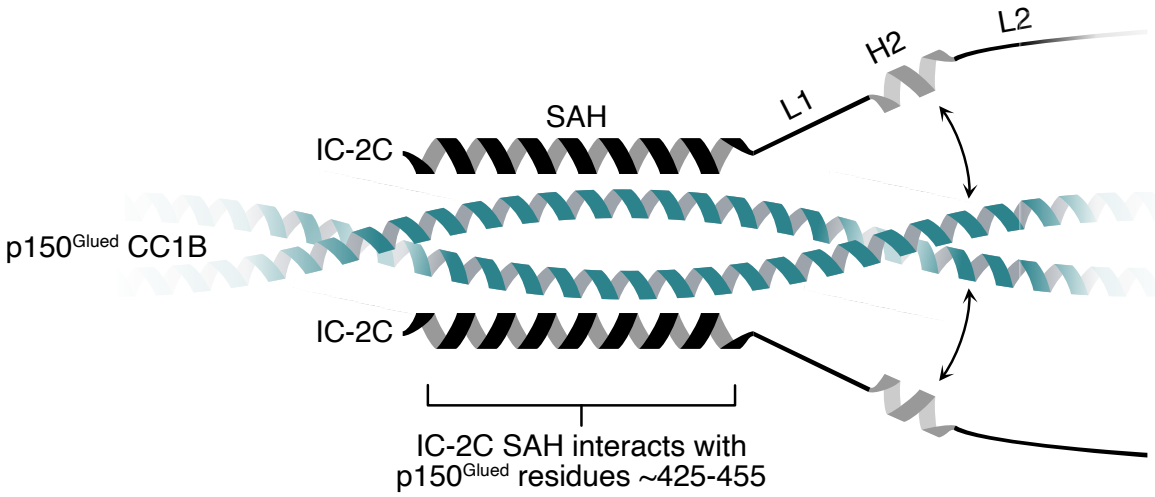

Figure 8. Model for the binding interaction between IC and p150^{Glued}. Our PRE and ITC results are best explained by a model in which the SAH regions of the IC monomers interact with approximately residues 425–455 of the p150^{Glued} CC1B dimer. The H2 region of IC is able to transiently interact with approximately residues 505–515 of the CC1B region but does not directly bind.

AlphaFold misidentifies the location of the p150^{Glued}/IC binding interaction and overpredicts structure

We tried using AlphaFold2 to predict the location at which p150^{Glued} and IC interact. As shown in Fig. 9a-c, the AlphaFold2 predictions consistently misidentify the location of binding when using constructs that matched what we used experimentally (p150$_{382-531}$ and IC-2C$_{1-96}$) as well as when shorter segments of the N-terminal region of IC were used (IC-2C$_{1-32}$ and IC-2C$_{1-44}$). The relatively favorable predicted local distance difference test (pLDDT), predicted aligned error (PAE), and predicted template modeling (pTM) scores from the AlphaFold2 predictions reflect that many parts of the secondary structure are correctly predicted and disguise the problem with the quaternary structure prediction. The main hints that the p150^{Glued}/IC interaction is mislocated (other than the disagreement with experimental data) were that a few of the lower-ranked predictions (not shown) had IC binding to the same spot along p150^{Glued} but oriented differently and that the interface-predicted template modeling (ipTM) scores were middling. Typically, ipTM scores above 0.8 correspond to high-quality predictions, values below 0.6 suggest failed predictions, and values between 0.6 and 0.8 are considered a "gray" area. The successively lower values for the ipTM scores for predictions using longer constructs of IC (going from IC-2C$_{1-32}$ to IC-2C$_{1-44}$ to IC-2C$_{1-96}$), despite identical structural predictions about the p150^{Glued}/IC interface, are because the inclusion of intrinsically disordered regions (such as the L2 region of IC) with low pLDDT scores negatively impacts the ipTM score.

AlphaFold2 also predicted that the disordered linker (L1) between the SAH and H2 regions forms an α-helix when bound to p150^{Glued}. That prediction is inconsistent with the NMR titration shown in Fig. 5a, as the rate at which peaks from amides in the L1 and H2 regions of IC-2C disappear as p150$_{382-531}$ was titrated into the sample should more closely match the rate of disappearance for peaks from the SAH region if, as predicted by AlphaFold2, residues 3-66 of IC-2C form one continuous helix when bound to p150^{Glued}. This overprediction of secondary structure for the L1 region of IC also occurred when AlphaFold2 was used to predict the structure

of monomeric IC-2C$_{1-96}$, as shown in Fig. 9d. This contradicts experimental results from NMR spectroscopy that unambiguously show that this region is disordered (16). For monomeric IC-2C$_{1-96}$, the lower pLDDT score from AlphaFold2 provides some hints that the L1 region in the predicted structure is incorrect, and the low pTM score also reflects low confidence in the structure (pTM scores less than 0.5 often indicate incorrect structures). Finally, we repeated all structure prediction calculations with AlphaFold3 and observed nearly identical results (data not shown).

Our general conclusion is that great care is needed when interpreting AlphaFold2 and AlphaFold3 predictions when studying proteins with intrinsically disordered regions or predicting binding between proteins. Although AlphaFold can be a useful complement to experimental data, pLDDT, PAE, pTM, and ipTM scores on their own are not always sufficient to identify mispredictions. Extra caution needs to be used when predicting protein binding, as AlphaFold will obligingly generate multimeric structures when asked to do so even if the resulting structures have no basis in reality. For example, the N-terminal region of IC is known to be monomeric in the absence of dynein light chain binding partners (27, 49), but, when asked to predict the structure for two copies of IC-2C$_{1-96}$, AlphaFold will try to find some way for them to interact as shown in Fig. 9e. Fortunately, in the case of "dimeric" IC-2C$_{1-96}$, the low pTM and ipTM scores serve as warnings that the predicted structure is not reliable. However, as seen in Fig. 9a, it is quite possible for AlphaFold to predict incorrect interactions with seemingly high confidence because the scores can be dominated by parts of the structure that are more reliable.

AlphaFold2 results potentially misdirected the fitting of Cryo-EM data

Recent work using cryo-EM data to generate models of the dynein/dynactin complex has suggested that the site of IC-2C binding on p150^{Glued} is approximately 25 residues closer to the C-terminus of the p150^{Glued} CC1B region (30) than where we have localized it based on our NMR data. We believe this discrepancy is explained by the use of AlphaFold2 as a guide for interpreting the cryo-EM data. As shown in Fig. 9a-c, AlphaFold2 incorrectly predicts the location of p150^{Glued}/IC binding, and, when using small segments of the N-terminal region of IC for the AlphaFold2 prediction (as was done for interpreting the cryo-EM data), the scores from the prediction are high enough that it is not immediately obvious that the prediction is unreliable.

As a consequence of using AlphaFold's misprediction, we believe that the prior work fitting cryo-EM data (30) has reached the wrong conclusion about the location of the IC binding site along the p150^{Glued} CC1B region. In the cryo-EM model, the N-terminal region of LIS1 binds p150^{Glued} at residues 420-455 (which is where we believe IC binds based on our NMR data), and the N-terminal region of IC binds p150^{Glued} at residues 458-478. The N-terminal regions of both LIS1 and IC are α-helical, so we believe that the simplest explanation for the discrepancy between our data and the cryo-EM model is that the identities of N-IC and N-LIS1 are swapped in the cryo-EM model.

An alternate explanation is that the p150^{Glued} CC1B region is mispositioned in the cryo-EM-based structure. Due to the repetitive nature of coiled-coil structures and the limited resolution of the cryo-EM data, it could be that the sequence for the CC1B region is incorrectly threaded through the density map (i.e., the coiled-coil is shifted too far in one direction in the structure). However, such a large misregistration of the coiled-coil seems less likely as an explanation for the discrepancy between our NMR-based results and the cryo-EM results as other features of p150^{Glued} (such as the CC1A and ICD regions) geometrically constrain where CC1B can be positioned in the structure.

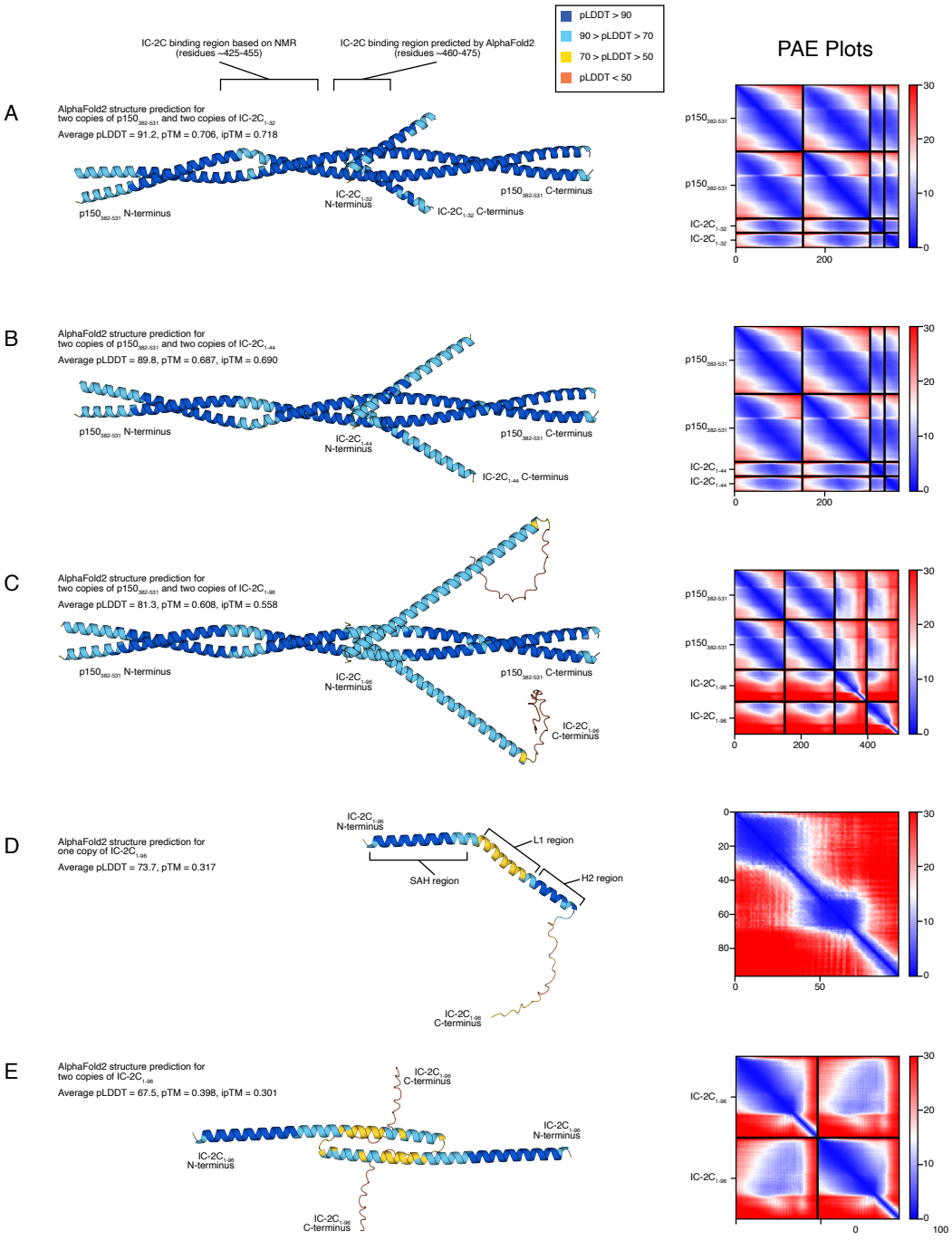

Figure 9. AlphaFold2 mispredicts the binding interaction between IC and p150Glued. Shown are AlphaFold2 predictions for two copies of $p150_{382-531}$ with two copies of IC-$2C_{1-32}$ (a), IC-$2C_{1-44}$ (b), or IC-$2C_{1-96}$ (c) as well as predictions for monomeric IC-$2C_{1-96}$ (d) and dimeric IC-$2C_{1-96}$ (e). Structure predictions are oriented with the N-termini at the left and colored according to the predicted local distance difference test (pLDDT). At right are the corresponding predicted aligned error (PAE) graphs for each AlphaFold2 prediction (with values in Å). For each prediction, only the top-ranking result of five calculations is shown. Cartoon structures rendered using PyMOL (50).

Conclusions

In this work, we have demonstrated that IC-2C binds to the p150^{Glued} CC1B region between residues 425 and 455. This finding contradicts a recent cryo-EM model for dynein/dynactin binding, which we believe is explained by the use of unreliable results from AlphaFold2 predictions to guide building the cryo-EM model. In addition, we have unambiguously shown that, in contrast to what has been observed in other organisms, the H2 region of mammalian IC is not involved in binding p150^{Glued}. Finally, in contrast to a previous report, we have shown that the S84D phosphomimetic mutation of IC-2C does not alter its binding to p150^{Glued}. Our work highlights some of the challenges of working with small constructs of structured proteins and in studying relatively weak interactions, as careful consideration of construct choice, sample conditions (temperature, pH, ionic strength), sample purity, and experimental technique are needed to ensure reliable results.

Going forward, we plan to extend our work to studying larger constructs of IC and p150^{Glued} to better understand the binding stoichiometry of these proteins, to help resolve the role of phosphorylation, and to better understand the role of autoinhibition in regulating these proteins (as has been suggested for CT variants of these proteins (51)). In particular, we believe that complexes that include IC's light chain binding partners will help provide insights into how the dynein and the dynein/dynactin complexes are regulated and assembled.

Methods

Protein sequences

Plasmid for generating recombinant *Homo sapiens* p150$_{382-531}$ (residues 382-531 of the p150^{Glued} CC1B region) was a gift from Elisar Barbar (Oregon State University). The sequence for this construct corresponds to entry Q14203 (DCTN1_HUMAN) in the UniProt protein database (52) and is 100% identical to the corresponding region for *Rattus norvegicus* (residues 381-530 for UniProt P28023, DCTN1_RAT). This initial p150^{Glued} construct had been previously prepared by PCR and cloned into a pET-24 vector with an N-terminal 6×His affinity purification tag using the Gibson Assembly protocol (53, 54). As a result, our initial p150^{Glued} construct included a four amino acid (GAHM) N-terminal cloning artifact that remained after tobacco etch virus (TEV) protease cleavage of the 6×His tag. All single-cysteine mutants of p150$_{382-531}$ were derived from this initial construct via site-directed mutagenesis and therefore retained the GAHM artifact. Subsequently, site-directed mutagenesis was used to remove this artifact, resulting in a p150$_{382-531}$ wild-type (WT) construct that had only native residues after TEV protease cleavage.

The sequence for IC-2C$_{1-96}$ for *Rattus norvegicus* was obtained from UniProt (Q62871-3, DC1I2_RAT). Residues 1-96 of IC-2C from *Rattus norvegicus* are 94.8% identical (five non-identical amino acids) with this region of IC-2C from *Homo sapiens* (Q13409-3, DC1I2_HUMAN) and were used to allow for comparison with previous research. The genes for IC-2C$_{1-96}$ and IC-2C$_{38-96}$ were synthesized and cloned into pET-24 plasmids by Genewiz (Azenta Life Sciences). These constructs have an N-terminal 6×His tag followed by a TEV protease cleavage site and were designed to have only native residues after TEV protease cleavage. Site-directed mutagenesis was used to generate the IC-2C$_{1-96}$ S84D mutant.

Isothermal titration calorimetry (ITC) and circular dichroism (CD) spectroscopy with protein samples of p150$_{382-531}$ and IC-2C$_{1-96}$ with and without the GAHM artifact established that

these additional amino acids had no impact on experimental outcomes (data not shown). DNA sequences for all plasmids were verified by Sanger sequencing before transformation into *Escherichia coli (E. coli)* BL21(DE3) cells for protein expression, from which glycerol stocks were made and stored at –80°C.

Protein expression

For all constructs of IC-2C$_{1\text{-}96}$, pre-cultures were made by inoculating 100 mL of MDG media (55) with scrapings from glycerol stocks and grown overnight at 37°C. Following incubation, these cultures were pelleted via centrifugation (3000×g, 10 min), and the resulting pellets were resuspended in 25 mL of ^{15}N-labeled MJ9 minimal media (56). Pelleting via centrifugation and resuspension in ^{15}N-labeled MJ9 media was repeated, and the resulting cell suspensions were then used to inoculate 1 L cultures of ^{15}N-labeled MJ9 media. The initial OD$_{600}$ (typically 0.5-0.8 at this point) was determined using a NanoDrop 2000c spectrometer (Thermo Fisher Scientific), after which the cultures were grown at 37°C until the OD$_{600}$ approximately doubled. At this point, isopropyl-β-D-1-thiogalactopyranoside (IPTG) was added to a final concentration of 0.4 mM to induce protein expression, and the cultures were grown for another 4-6 h.

The p150$_{382\text{-}531}$ constructs were grown by inoculating 250 mL cultures of ZYM-5052 auto-inducing media (55) with scrapings from glycerol stocks and then grown at 25°C for ~60 h. Both the IC-2C$_{1\text{-}96}$ and the p150$_{382\text{-}531}$ cultures were harvested via centrifugation (3,000×g, 20 min), and the resulting cell pellets were stored at –20°C. All bacterial growth media contained kanamycin at 50 μg L^{-1} to maintain the expression plasmids.

Protein purification

Thawed cell pellets were resuspended in ice-cold lysis buffer (250 mM sodium chloride, 20 mM imidazole, 20 mM sodium phosphate buffer [pH 7.4], 1× protease inhibitor cocktail) and lysed by ultrasonication. For single-cysteine mutants, 1-2 mM dithiothreitol (DTT) was included in the lysis buffer as well as in buffers used for subsequent purification steps unless otherwise noted. The resulting lysates were clarified by high-speed centrifugation (42,000×g, 30 min, 4°C) and then passed through 0.45 μm filters prior to chromatography.

Proteins were purified from clarified lysates after filtering through 0.45 μm syringe filters by immobilized metal affinity chromatography (IMAC) using an ÄKTAprime plus liquid chromatography system (Cytiva Life Sciences) with a 5 mL HisTrap HP column (Cytiva Life Sciences). Binding buffer (20 mM imidazole, 500 mM sodium chloride, 20 mM sodium phosphate buffer [pH 7.4]) was used to wash the column before gradient elution with a high imidazole concentration buffer (500 mM imidazole, 500 mM sodium chloride, 20 mM sodium phosphate buffer [pH 7.4]). Fractions from IMAC and subsequent purification steps were analyzed by sodium dodecyl sulfate-polyacrylamide gel electrophoresis (SDS-PAGE) to verify the expression and purity of the target proteins.

His-tagged TEV protease (57) was added at approximately a ratio of 1:100 (TEV to target protein) to IMAC fractions containing the target proteins to cleave the N-terminal 6×His-tags from the proteins. Samples were then dialyzed overnight at 4°C using 3.5 kDa molecular weight cut-off (MWCO) dialysis tubing against TEV cleavage buffer (50 mM NaCl, 20 mM sodium phosphate buffer [pH 7.4]). For samples for which the cleavage was still incomplete at this point (as determined by SDS-PAGE), the samples were concentrated with Amicon Ultra-15 centrifugal filters (Millipore), fresh TEV protease was added, and the mixture was allowed to incubate overnight at room temperature.

TEV-cleaved protein samples were filtered using 0.45 µm syringe filters and then passed over His GraviTrap columns (Cytiva Life Sciences). The flow through (containing the TEV-cleaved target protein) was collected along with binding buffer (20 mM imidazole, 500 mM sodium chloride, 20 mM sodium phosphate buffer [pH 7.4]) that was subsequently used to wash the target protein from the column. The column was then washed with reverse IMAC wash buffer (75 mM imidazole, 500 mM sodium chloride, 20 mM sodium phosphate buffer [pH 7.4]), after which proteins that bound to the column (6×His-tag, His-tagged TEV protease, bacterial proteins that bind to nickel columns) were eluted with elution buffer (500 mM imidazole, 500 mM sodium chloride, 20 mM sodium phosphate buffer [pH 7.4]).

Reverse IMAC fractions containing target protein were concentrated using Amicon Ultra-15 centrifugal filters to volumes of around 1 mL. Concentrated protein samples were filtered with 0.22 µm syringe filters and then further purified by size exclusion chromatography (SEC) using an ÄKTAprime plus system with a HiPrep 16/60 Sephacryl S-100 High Resolution gel filtration column (Cytiva Life Sciences). The buffer used for SEC contained 150 mM sodium chloride and 50 mM sodium phosphate buffer (pH 7.4). For single-cysteine mutants, 1 mM tris(2-carboxyethyl)phosphine (TCEP) was included in the SEC buffer to keep the cysteine in a reduced state.

Protein quantification

Protein concentrations were determined by measuring the absorbance at 205 and 280 nm using a NanoDrop 2000c spectrometer (Thermo Fisher Scientific). Molar extinction coefficients for absorbance measurements at 205 and 280 nm were computed with a protein calculator tool (48).

After cleavage with TEV protease, the molar extinction coefficient at 280 nm (ε_{280}) for IC-2C$_{1\text{-}96}$ is 0 M^{-1} cm^{-1} (no tyrosines or tryptophans) and for p150$_{382\text{-}531}$ is only 1490 M^{-1} cm^{-1} (one tyrosine, no tryptophans). Consequently, we used the combination of the A_{205} and A_{280} measurements to correct our estimates of IC-2C$_{1\text{-}96}$ and p150$_{382\text{-}531}$ concentrations using the following equation:

$$[\text{protein}] = \frac{A_{205} - (30 \times A_{280})}{\varepsilon_{205} - (30 \times \varepsilon_{280})} \quad (2)$$

where ε_{205} and ε_{280} are the molar extinction coefficients at 205 and 280 nm for the target protein (IC-2C$_{1\text{-}96}$ or p150$_{382\text{-}531}$). This equation corrects for the potential presence of contaminant proteins which may lead to anomalously high A_{280} values compared to the A_{205} values (see Supplementary Materials for a derivation of this equation). For example, as IC-2C$_{1\text{-}96}$ does not absorb at 280 nm, a non-zero A_{280} indicates the presence of other contaminants that should be subtracted from the A_{205} value to get a more accurate concentration estimate. Although p150$_{382\text{-}531}$ does absorb weakly at A_{280}, this equation can still be used to correct its concentration. The factor of 30 in this equation assumes that any contaminant proteins have an average number of tryptophans and tyrosines (48); that is, $\varepsilon_{205}/\varepsilon_{280} \approx 30$ for "average" proteins.

Paramagnetic labeling with MTSL

After purification, a 5 mL HiTrap desalting column (Cytiva Life Sciences) was used to buffer exchange single-cysteine mutants into MTSL labeling buffer (50 mM sodium chloride, 50 mM sodium phosphate buffer [pH 8]). Fractions containing protein were combined and concentrated to less than 1 mL using Amicon Ultra-4 centrifugal filters. Protein samples were allowed to react with the paramagnetic label *S*-(1-oxyl-2,2,5,5-tetramethyl-2,5-dihydro-1H-pyrrol-3-yl)methyl methanesulfonothioate (MTSL) in a 20:1 ratio (MTSL to target protein) for at least 2 h in the dark

at room temperature. The MTSL-labeled proteins were then buffer exchanged into SEC buffer (150 mM sodium chloride, 50 mM sodium phosphate buffer [pH 7.4]) using a 5 mL HiTrap desalting column, and, after further concentration, the protein concentration of the resulting stock was quantified by measuring the A_{205} and A_{280} values. The MTSL label and the disulfide bond attaching the label to the protein increase ε_{280} by approximately 825 M^{-1} cm^{-1} (58).

Nuclear magnetic resonance (NMR) spectroscopy

NMR spectra for studying IC-2C$_{1-96}$/p150$_{382-531}$ and IC-2C$_{38-96}$/p150$_{382-531}$ interactions were collected with a sample temperature of 10°C using an Avance NEO 600 MHz spectrometer (Bruker BioSpin) with a TXI room-temperature probe. The buffer for all NMR samples consisted of 150 mM sodium chloride, 50 mM sodium phosphate (pH 7.4), 5% D_2O, and 0.2 mM DSS (sodium 3-(trimethylsilyl)propane-1-sulfonate). For determining the optimal ratio for measuring PREs, NMR samples consisted of 600 μM ^{15}N-labeled IC-2C$_{1-96}$ WT with varying concentrations of MTSL-labeled p150$_{382-531}$ L434C. For all other IC/p150^{Glued} intermolecular PRE experiments, NMR samples consisted of 600 μM ^{15}N-labeled IC-2C$_{1-96}$ WT and 15 μM MTSL-labeled p150$_{382-531}$ single-cysteine mutants.

Backbone chemical shift assignments were previously determined using a ^{13}C,^{15}N-labeled sample of IC-2C$_{1-96}$ at 15ºC and in a buffer containing 50 mM NaCl and 10 mM sodium phosphate (pH 6.0) (16). Using these assignments as a starting point, the chemical shift assignments were transferred to the sample conditions used in this study (150 mM NaCl, 50 mM phosphate pH 7.4, 10ºC). The resulting backbone chemical shift assignments for IC-2C$_{1-96}$ WT were deposited at the Biological Magnetic Resonance Bank (BMRB: 53249).

For each MTSL-labeled sample, proton transverse relaxation rates (^{1}H R_2) were determined when the MTSL label was in the paramagnetic state using a variant of a previously-proposed ^{1}H R_2 measurement experiment (59). In our version of this experiment, band-selective pulses are used for all proton pulses, which allows shorter recycle delays to be used. The variable delay time during the first INEPT step of the pulse sequence, which results in relaxation weighting of the NMR signal intensities, was varied between 0 and 30 ms. After acquiring the initial ^{1}H R_2 measurement experiment, the MTSL label was reduced to the diamagnetic state by adding ascorbate to the samples to a final concentration of 4.3 mM. After allowing the ascorbate to reduce the MTSL for 2 h at room temperature, the experiment was repeated to determine ^{1}H R_2 values for the diamagnetic state.

NMR data were processed using TopSpin 4.5.0 (Bruker BioSpin) and analyzed using CCPN Analysis 2.5.2 (60). Peak heights were determined using a parabolic fit, and the change in peak height with increasing delay time for each peak was fit to an exponential function to determine the decay rate (R_2) with errors estimated using a covariance method.

Circular dichroism (CD) Spectroscopy

A J-810 spectropolarimeter (JASCO) with a 1 mm pathlength quartz glass cuvette was used to acquire CD spectra of protein samples at concentrations of 10-20 μM. Spectra were acquired from 260 to 195 nm with a bandwidth of 2 nm and a scanning rate of 10 nm/min at temperatures ranging from 5 to 50°C in 5°C intervals. Denaturation midpoint temperatures (T_m) were estimated by fitting the average mean ellipticity (mdeg) from 220 to 224 nm for each sample at each temperature to a two-site (N ⇌ D) model using CDpal (61).

Isothermal titration calorimetry (ITC)

Prior to ITC, Amicon Ultra-0.5 centrifugal filters were used to buffer exchange protein samples into the same batch of SEC buffer (150 mM sodium chloride, 50 mM sodium phosphate [pH 7.4]). Unless otherwise noted, all ITC experiments were conducted using a MicroCal iTC200 system (Malvern Instruments) and fit to a one set of sites model using Origin 7 (OriginLabs). Each experiment was started with a 1 μL injection followed by 18 injections of 2 μL. The dimerization constant of $p150_{382\text{-}531}$ WT was measured by ITC at temperatures ranging from 5 to 30°C. For these experiments, $p150_{382\text{-}531}$ WT at a concentration of 400–500 μM in the syringe was titrated into SEC buffer in the cell. For experiments studying the binding interactions between IC-$2C_{1\text{-}96}$ constructs and $p150_{382\text{-}531}$ constructs (including MTSL-labeled single-cysteine mutants of $p150_{382\text{-}531}$), IC-$2C_{1\text{-}96}$ constructs at a concentration of 350–400 μM in the syringe were titrated into $p150_{382\text{-}531}$ constructs at a concentration of 25–55 μM in the cell at 15°C.

AlphaFold predictions

AlphaFold2 structure predictions were carried out using a local installation of ColabFold 1.5.5 (62) and a remote server for MMseqs2 (63). Structures of single chains were predicted with AlphaFold2 (64) and the structures of complexes were predicted with AlphaFold2-Multimer (65). Structure predictions were replicated with AlphaFold3 using the AlphaFold Server (47).

Supporting Information

Figure S1. Circular dichroism spectroscopy of MTSL-labeled single-cysteine $p150_{382\text{-}531}$ mutants.

Figure S2. Thermograms and binding isotherms for the binding of IC-$2C_{1\text{-}96}$ with wild-type $p150_{382\text{-}531}$ and MTSL-labeled single-cysteine $p150_{382\text{-}531}$ mutants.

Figure S3. The binding affinity of $p150_{382\text{-}531}$ to IC-$2C_{1\text{-}96}$ does not vary with concentration.

Figure S4. Proton transverse relaxation data for amides of IC-$2C_{1\text{-}96}$ in the presence of different substoichiometric amounts of $p150_{382\text{-}531}$.

Figure S5. Proton transverse relaxation data for amides of IC-$2C_{1\text{-}96}$ in the presence of MTSL-labeled $p150_{382\text{-}531}$ mutants.

Derivation of equation 2 from the text.

Acknowledgements

We thank Elisar Barbar and her research group at Oregon State University for their advice and support, for providing some of the initial plasmids used for this research, and for providing access to their MicroCal VP-ITC instrument (Malvern Instruments). In addition, we thank Jack Allen, Kailey Aiona, Sawyer Barta, Benjamin Bromberg, Juliana Choza, Hannah Creasey, Will Gattiker, Nhi Ho, Annie Kingsland, Malina Kobayashi, Zack Kon, Lejla Krečinić-Balić, Noah Merz, Casey Myszkowski, David Nhek, Dylan Ramsden, Arundhati Suresh, Kate Saylor, and Asia Wooten, who, as part of the Lewis & Clark College biochemistry lab course, designed and generated many of the single-cysteine p150^{Glued} mutants used in this project. We acknowledge support from the National Science Foundation (Award 2003557). S.M.D., B.L.D., D.M., and A.C.M. received support from the Lewis & Clark College John S. Rogers Science Research Program. The Lewis & Clark College 600 MHz NMR spectrometer was purchased with support from the National Science Foundation (Award 1917696) and the M. J. Murdock Charitable Trust (Grant 201811283).

References

1. Kardon, J. R., and Vale, R. D. (2009) Regulators of the cytoplasmic dynein motor. *Nat Rev Mol Cell Biol*. **10**, 854–865
2. Vallee, R. B., McKenney, R. J., and Ori-McKenney, K. M. (2012) Multiple modes of cytoplasmic dynein regulation. *Nat Cell Biol*. **14**, 224–230
3. Reck-Peterson, S. L., Redwine, W. B., Vale, R. D., and Carter, A. P. (2018) The cytoplasmic dynein transport machinery and its many cargoes. *Nat. Rev. Mol. Cell Biol.* **19**, 382–398
4. Kini, A. R., and Collins, C. A. (2001) Modulation of cytoplasmic dynein ATPase activity by the accessory subunits. *Cell Motil Cytoskeleton*. **48**, 52–60
5. Carter, A. P., Garbarino, J. E., Wilson-Kubalek, E. M., Shipley, W. E., Cho, C., Milligan, R. A., Vale, R. D., and Gibbons, I. R. (2008) Structure and functional role of dynein's microtubule-binding domain. *Science*. **322**, 1691–1695
6. McKenney, R. J., Huynh, W., Tanenbaum, M. E., Bhabha, G., and Vale, R. D. (2014) Activation of cytoplasmic dynein motility by dynactin-cargo adapter complexes. *Science*. **345**, 337–341
7. Makokha, M., Hare, M., Li, M., Hays, T., and Barbar, E. (2002) Interactions of cytoplasmic dynein light chains Tctex-1 and LC8 with the intermediate chain IC74. *Biochemistry*. **41**, 4302–4311
8. Nyarko, A., and Barbar, E. (2011) Light chain-dependent self-association of dynein intermediate chain. *J Biol Chem*. **286**, 1556–1566
9. Nyarko, A., Song, Y., and Barbar, E. (2012) Intrinsic disorder in dynein intermediate chain modulates its interactions with NudE and dynactin. *J Biol Chem*. **287**, 24884–24893
10. Pfister, K. K. (2015) Distinct functional roles of cytoplasmic dynein defined by the intermediate chain isoforms. *Exp Cell Res*. **334**, 54–60
11. Mikami, A., Paschal, B. M., Mazumdar, M., and Vallee, R. B. (1993) Molecular cloning of the retrograde transport motor cytoplasmic dynein (MAP 1C). *Neuron*. **10**, 787–796
12. Vaughan, K. T., Mikami, A., Paschal, B. M., Holzbaur, E. L., Hughes, S. M., Echeverri, C. J., Moore, K. J., Gilbert, D. J., Copeland, N. G., Jenkins, N. A., and Vallee, R. B. (1996) Multiple mouse chromosomal loci for dynein-based motility. *Genomics*. **36**, 29–38
13. Kuta, A., Deng, W., Morsi El-Kadi, A., Banks, G. T., Hafezparast, M., Pfister, K. K., and Fisher, E. M. C. (2010) Mouse cytoplasmic dynein intermediate chains: identification of new isoforms, alternative splicing and tissue distribution of transcripts. *PLoS One*. **5**, e11682
14. Vaughan, K. T., and Vallee, R. B. (1995) Cytoplasmic dynein binds dynactin through a direct interaction between the intermediate chains and p150^{Glued}. *J. Cell Biol.* **131**, 1507–1516
15. Myers, K. R., Lo, K. W.-H., Lye, R. J., Kogoy, J. M., Soura, V., Hafezparast, M., and Pfister, K. K. (2007) Intermediate chain subunit as a probe for cytoplasmic dynein function: biochemical analyses and live cell imaging in PC12 cells. *J. Neurosci. Res.* **85**, 2640–2647
16. Jie, J., Löhr, F., and Barbar, E. (2017) Dynein Binding of Competitive Regulators Dynactin and NudE Involves Novel Interplay between Phosphorylation Site and Disordered Spliced Linkers. *Structure*. **25**, 421–433
17. Schroer, T. A. (2004) Dynactin. *Annu. Rev. Cell Dev. Biol.* **20**, 759–779
18. Boylan, K. L. M., and Hays, T. S. (2002) The gene for the intermediate chain subunit of cytoplasmic dynein is essential in Drosophila. *Genetics*. **162**, 1211–1220

19. Gepner, J., Li, M., Ludmann, S., Kortas, C., Boylan, K., Iyadurai, S. J., McGrail, M., and Hays, T. S. (1996) Cytoplasmic dynein function is essential in Drosophila melanogaster. *Genetics*. **142**, 865–878
20. Ansar, M., Ullah, F., Paracha, S. A., Adams, D. J., Lai, A., Pais, L., Iwaszkiewicz, J., Millan, F., Sarwar, M. T., Agha, Z., Shah, S. F., Qaisar, A. A., Falconnet, E., Zoete, V., Ranza, E., Makrythanasis, P., Santoni, F. A., Ahmed, J., Katsanis, N., Walsh, C., Davis, E. E., and Antonarakis, S. E. (2019) Bi-allelic variants in DYNC1I2 cause syndromic microcephaly with intellectual disability, cerebral malformations, and dysmorphic facial features. *Am J Hum Genet*. **104**, 1073–1087
21. Morel, M., Héraud, C., Nicaise, C., Suain, V., and Brion, J.-P. (2012) Levels of kinesin light chain and dynein intermediate chain are reduced in the frontal cortex in Alzheimer's disease: implications for axoplasmic transport. *Acta Neuropathol*. **123**, 71–84
22. Lipka, J., Kuijpers, M., Jaworski, J., and Hoogenraad, C. C. (2013) Mutations in cytoplasmic dynein and its regulators cause malformations of cortical development and neurodegenerative diseases. *Biochem Soc Trans*. **41**, 1605–1612
23. Vaughan, P. S., Leszyk, J. D., and Vaughan, K. T. (2001) Cytoplasmic dynein intermediate chain phosphorylation regulates binding to dynactin. *J. Biol. Chem.* **276**, 26171–26179
24. Whyte, J., Bader, J. R., Tauhata, S. B. F., Raycroft, M., Hornick, J., Pfister, K. K., Lane, W. S., Chan, G. K., Hinchcliffe, E. H., Vaughan, P. S., and Vaughan, K. T. (2008) Phosphorylation regulates targeting of cytoplasmic dynein to kinetochores during mitosis. *J Cell Biol*. **183**, 819–834
25. King, S. J., Brown, C. L., Maier, K. C., Quintyne, N. J., and Schroer, T. A. (2003) Analysis of the dynein-dynactin interaction in vitro and in vivo. *Mol Biol Cell*. **14**, 5089–5097
26. Morgan, J. L., Song, Y., and Barbar, E. (2011) Structural dynamics and multiregion interactions in dynein-dynactin recognition. *J. Biol. Chem.* **286**, 39349–39359
27. Siglin, A. E., Sun, S., Moore, J. K., Tan, S., Poenie, M., Lear, J. D., Polenova, T., Cooper, J. A., and Williams, J. C. (2013) Dynein and dynactin leverage their bivalent character to form a high-affinity interaction. *PLoS ONE*. **8**, e59453
28. Urnavicius, L., Zhang, K., Diamant, A. G., Motz, C., Schlager, M. A., Yu, M., Patel, N. A., Robinson, C. V., and Carter, A. P. (2015) The structure of the dynactin complex and its interaction with dynein. *Science*. **347**, 1441–1446
29. Tripathy, S. K., Weil, S. J., Chen, C., Anand, P., Vallee, R. B., and Gross, S. P. (2014) Autoregulatory mechanism for dynactin control of processive and diffusive dynein transport. *Nat Cell Biol*. **16**, 1192–1201
30. Singh, K., Lau, C. K., Manigrasso, G., Gama, J. B., Gassmann, R., and Carter, A. P. (2024) Molecular mechanism of dynein-dynactin complex assembly by LIS1. *Science*. **383**, eadk8544
31. Dyson, H. J., and Wright, P. E. (2005) Intrinsically unstructured proteins and their functions. *Nat Rev Mol Cell Biol*. **6**, 197–208
32. Dyson, H. J., and Wright, P. E. (2021) NMR illuminates intrinsic disorder. *Curr Opin Struct Biol*. **70**, 44–52
33. Schiavina, M., Bracaglia, L., Bolognesi, T., Rodella, M. A., Tagliaferro, G., Tino, A. S., Pierattelli, R., and Felli, I. C. (2024) Intrinsically disordered proteins studied by NMR spectroscopy. *Journal of Magnetic Resonance Open*. **18**, 100143
34. MacKay, J. P., Shaw, G. L., and King, G. F. (1996) Backbone dynamics of the c-Jun leucine zipper: ^{15}N NMR relaxation studies. *Biochemistry*. **35**, 4867–4877

35. Loening, N. M., and Barbar, E. (2021) Structural characterization of the self-association domain of swallow. *Protein Sci*. **30**, 1056–1063
36. Clore, G. M., and Iwahara, J. (2009) Theory, practice, and applications of paramagnetic relaxation enhancement for the characterization of transient low-population states of biological macromolecules and their complexes. *Chem Rev*. **109**, 4108–4139
37. Zhou, N. E., Kay, C. M., and Hodges, R. S. (1992) Synthetic model proteins. Positional effects of interchain hydrophobic interactions on stability of two-stranded alpha-helical coiled-coils. *Journal of Biological Chemistry*. **267**, 2664–2670
38. Loening, N. M., Saravanan, S., Jespersen, N. E., Jara, K., and Barbar, E. (2020) Interplay of disorder and sequence specificity in the formation of stable dynein-dynactin complexes. *Biophys J*. **119**, 950–965
39. Lupas, A., Van Dyke, M., and Stock, J. (1991) Predicting coiled coils from protein sequences. *Science*. **252**, 1162–1164
40. Simm, D., Hatje, K., and Kollmar, M. (2015) Waggawagga: comparative visualization of coiled-coil predictions and detection of stable single α-helices (SAH domains). *Bioinformatics*. **31**, 767–769
41. Delorenzi, M., and Speed, T. (2002) An HMM model for coiled-coil domains and a comparison with PSSM-based predictions. *Bioinformatics*. **18**, 617–625
42. Trigg, J., Gutwin, K., Keating, A. E., and Berger, B. (2011) Multicoil2: predicting coiled coils and their oligomerization states from sequence in the twilight zone. *PLoS One*. **6**, e23519
43. Lupas, A. (1996) Prediction and analysis of coiled-coil structures. *Methods Enzymol*. **266**, 513–525
44. McDonnell, A. V., Jiang, T., Keating, A. E., and Berger, B. (2006) Paircoil2: improved prediction of coiled coils from sequence. *Bioinformatics*. **22**, 356–358
45. Gruber, M., Söding, J., and Lupas, A. N. (2006) Comparative analysis of coiled-coil prediction methods. *J Struct Biol*. **155**, 140–145
46. Ludwiczak, J., Winski, A., Szczepaniak, K., Alva, V., and Dunin-Horkawicz, S. (2019) DeepCoil-a fast and accurate prediction of coiled-coil domains in protein sequences. *Bioinformatics*. **35**, 2790–2795
47. Abramson, J., Adler, J., Dunger, J., Evans, R., Green, T., Pritzel, A., Ronneberger, O., Willmore, L., Ballard, A. J., Bambrick, J., Bodenstein, S. W., Evans, D. A., Hung, C.-C., O'Neill, M., Reiman, D., Tunyasuvunakool, K., Wu, Z., Žemgulytė, A., Arvaniti, E., Beattie, C., Bertolli, O., Bridgland, A., Cherepanov, A., Congreve, M., Cowen-Rivers, A. I., Cowie, A., Figurnov, M., Fuchs, F. B., Gladman, H., Jain, R., Khan, Y. A., Low, C. M. R., Perlin, K., Potapenko, A., Savy, P., Singh, S., Stecula, A., Thillaisundaram, A., Tong, C., Yakneen, S., Zhong, E. D., Zielinski, M., Žídek, A., Bapst, V., Kohli, P., Jaderberg, M., Hassabis, D., and Jumper, J. M. (2024) Accurate structure prediction of biomolecular interactions with AlphaFold 3. *Nature*. **630**, 493–500
48. Anthis, N. J., and Clore, G. M. (2013) Sequence-specific determination of protein and peptide concentrations by absorbance at 205 nm. *Protein Sci*. **22**, 851–858
49. Jie, J., Löhr, F., and Barbar, E. (2015) Interactions of yeast dynein with dynein light chain and dynactin: general implications for intrinsically disordered duplex scaffolds in multiprotein assemblies. *J. Biol. Chem.* **290**, 23863–23874
50. The PyMOL Molecular Graphics System, Version 3.0

51. Jara, K. A., Loening, N. M., Reardon, P. N., Yu, Z., Woonnimani, P., Brooks, C., Vesely, C. H., and Barbar, E. J. (2022) Multivalency, autoinhibition, and protein disorder in the regulation of interactions of dynein intermediate chain with dynactin and the nuclear distribution protein. *Elife*. **11**, e80217
52. The UniProt Consortium (2023) UniProt: the universal protein knowledgebase in 2023. *Nucleic Acids Research*. **51**, D523–D531
53. Gibson, D. G., Young, L., Chuang, R.-Y., Venter, J. C., Hutchison, C. A., and Smith, H. O. (2009) Enzymatic assembly of DNA molecules up to several hundred kilobases. *Nat Methods*. **6**, 343–345
54. Gibson, D. G., Glass, J. I., Lartigue, C., Noskov, V. N., Chuang, R.-Y., Algire, M. A., Benders, G. A., Montague, M. G., Ma, L., Moodie, M. M., Merryman, C., Vashee, S., Krishnakumar, R., Assad-Garcia, N., Andrews-Pfannkoch, C., Denisova, E. A., Young, L., Qi, Z.-Q., Segall-Shapiro, T. H., Calvey, C. H., Parmar, P. P., Hutchison, C. A., Smith, H. O., and Venter, J. C. (2010) Creation of a bacterial cell controlled by a chemically synthesized genome. *Science*. **329**, 52–56
55. Studier, F. W. (2005) Protein production by auto-induction in high density shaking cultures. *Protein Expr Purif*. **41**, 207–234
56. Jansson, M., Li, Y. C., Jendeberg, L., Anderson, S., Montelione, G. T., and Nilsson, B. (1996) High-level production of uniformly ^{15}N- and ^{13}C-enriched fusion proteins in Escherichia coli. *J Biomol NMR*. **7**, 131–141
57. Davis, S. M., Romig, B. L., Abe, A. A., and Loening, N. M. (2025) An improved variant of tobacco etch virus (TEV) protease that does not need reducing agents. *Protein Sci*. **34**, e70049
58. Venditti, V., and Fawzi, N. L. (2018) Probing the atomic structure of transient protein contacts by paramagnetic relaxation enhancement solution NMR. *Methods Mol Biol*. **1688**, 243–255
59. Donaldson, L. W., Skrynnikov, N. R., Choy, W. Y., Muhandiram, D. R., Sarkar, B., Forman-Kay, J. D., and Kay, L. E. (2001) Structural characterization of proteins with an attached ATCUN motif by paramagnetic relaxation enhancement NMR spectroscopy. *J Am Chem Soc*. **123**, 9843–9847
60. Vranken, W. F., Boucher, W., Stevens, T. J., Fogh, R. H., Pajon, A., Llinas, M., Ulrich, E. L., Markley, J. L., Ionides, J., and Laue, E. D. (2005) The CCPN data model for NMR spectroscopy: Development of a software pipeline. *Proteins: Structure, Function, and Bioinformatics*. **59**, 687–696
61. Niklasson, M., Andresen, C., Helander, S., Roth, M. G. L., Zimdahl Kahlin, A., Lindqvist Appell, M., Mårtensson, L.-G., and Lundström, P. (2015) Robust and convenient analysis of protein thermal and chemical stability. *Protein Sci*. **24**, 2055–2062
62. Mirdita, M., Schütze, K., Moriwaki, Y., Heo, L., Ovchinnikov, S., and Steinegger, M. (2022) ColabFold: making protein folding accessible to all. *Nat Methods*. **19**, 679–682
63. Mirdita, M., Steinegger, M., and Söding, J. (2019) MMseqs2 desktop and local web server app for fast, interactive sequence searches. *Bioinformatics*. **35**, 2856–2858
64. Jumper, J., Evans, R., Pritzel, A., Green, T., Figurnov, M., Ronneberger, O., Tunyasuvunakool, K., Bates, R., Žídek, A., Potapenko, A., Bridgland, A., Meyer, C., Kohl, S. A. A., Ballard, A. J., Cowie, A., Romera-Paredes, B., Nikolov, S., Jain, R., Adler, J., Back, T., Petersen, S., Reiman, D., Clancy, E., Zielinski, M., Steinegger, M., Pacholska, M., Berghammer, T., Bodenstein, S., Silver, D., Vinyals, O., Senior, A. W., Kavukcuoglu, K.,

Kohli, P., and Hassabis, D. (2021) Highly accurate protein structure prediction with AlphaFold. *Nature*. **596**, 583–589

65. Evans, R., O'Neill, M., Pritzel, A., Antropova, N., Senior, A., Green, T., Žídek, A., Bates, R., Blackwell, S., Yim, J., Ronneberger, O., Bodenstein, S., Zielinski, M., Bridgland, A., Potapenko, A., Cowie, A., Tunyasuvunakool, K., Jain, R., Clancy, E., Kohli, P., Jumper, J., and Hassabis, D. (2022) Protein complex prediction with AlphaFold-Multimer. 10.1101/2021.10.04.463034